Supplementary Information

A non-van der Waals platform for deep-subwavelength twist-polaritonics based on β-Ga_2O_3 nanoflakes

Liyan Wang,[a] Kaijun Feng,[b] Shuai Liu,[c] Jiehui Tian,[a] Xiangdong Guo,[b] Lin Geng,[c] Yuchuan Xiao,[d] Debo Hu,*[a] Lixing Kang*[c] and Qing Dai*[b]

[a] Laboratory of Nanophotonic Materials and Devices, Laboratory of Standardization and Measurement for Nanotechnology, National Centre for Nanoscience and Technology, Beijing 100190, China. E-mail: hudb@nanoctr.cn
[b] School of Materials Science and Engineering, Shanghai Jiao Tong University, Shanghai, China. E-mail: daiqing@sjtu.edu.cn
[c] Division of Advanced Materials, Suzhou Institute of Nano-Tech and Nano-Bionics, Chinese Academy of Sciences, Suzhou 215123, China. E-mail: lxkang2013@sinano.ac.cn
[d] Suzhou Laboratory, Suzhou, 215100, China.

Table S1. Interlayer binding energy of representative 2D materials

Materials	Interlayer binding energy (meV·Å^{-2})	Interaction strength	Structure	References	
Graphene	22.5	weak vdW interaction		1	
*h*BN	25.0		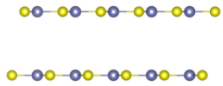	1	
WSe_2	25.6		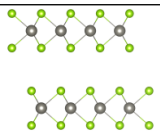	1	
WS_2	26.1		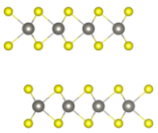	1	
MoS_2	26.3		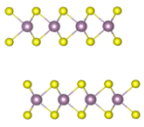	1	
CrSBr	27.17		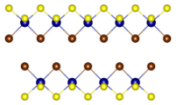	2	
V_2O_5	28.8		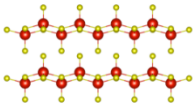	2	
$CaSO_4.2H_2O$	28.4	weak non-vdW interaction	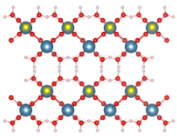	2	
β-Ga_2O_3-(100)B	30.58		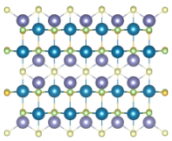	3	
P (black)	33.4	strong vdW interaction	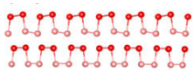	1	
SnS	36.5	strong vdW interaction	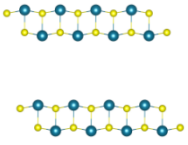	1	

Table S2. Classification of non-vdW layered cleavable materials and typical representatives

Major Category	Subclass Name	Structural Feature	Dominant Interlayer Interaction	Typical Representatives	References
Ionic Bond-Dominated Type (Most abundant in nature)	Charge-Compensating Cation Group	Negatively charged covalent-ionic framework layers + interlayer large-radius cations	Ionic bonds between cations and framework oxygen atoms	Mica, KBBF ($KBe_2BO_3F_2$)	4 5
	Charge-Compensating Anion Group (LDHs Family)	Positively charged metal hydroxide layers + interlayer exchangeable anions	Long-range electrostatic attraction between charged layers and counterions	Hydrotalcite	4
Hydrogen Bond-Dominated Type	Crystalline WaterMediated Hydrogen Bond Group	Strong ionic bond framework layers + interlayer crystalline water molecule layers	Hydrogen bonds between water molecules and framework	Gypsum ($CaSO_4 \cdot 2H_2O$)	6
	Hydroxyl-Mediated Hydrogen Bond Group	Framework surface hydroxyl groups directly bond to oxygen atoms of adjacent layers	Hydroxyl-oxygen hydrogen bonds	Lepidocrocite (γ-FeO(OH)), Atacamite ($Cu_2Cl(OH)_3$)	4
Weak Metallic Bond-Dominated Type (Artificial Synthesize)	MAX Phases (Ternary Carbides / Nitrides)	General formula $M_{n+1}AX_n$, strong M-X covalent bond layers + weak M-A metallic bond layers	Weak M-A metallic bonds	Ti_3AlC_2, Ti_2AlC, Nb_4AlC_3	7
	MAB Phases (Ternary Borides)	General formula $M_{n+1}AB_{2n}$, strong M-B covalent bond layers + weak M-A metallic bond layers	Weak M-A metallic bonds	Ti_2InB_2, Zr_2SB_2, Hf_2PB_2	8
Weak Covalent Bond-Dominated Type	Semiconductor / Transition Metal Oxides	Stacking of independent metal oxygen polyhedron 2D layers	Weak covalent bonds + partial ionic bonds	γ-WO_3, SnO, β-Ga_2O_3	9 10 3
	Other Emerging Layered Materials	Diverse layered framework structures	Weak covalent bonds / weak metallic bonds	Bi_2O_2Se, MgB_2, KV_3Sb_5	10

Table S3. Comparison of key polariton performance metrics for β-Ga_2O_3 and other representative polaritonic platforms

Material	Crystal orientation	Polaritons type	Frequency range (cm^{-1})	Thickness (nm)	Re(k_p/k_0)	*Q*	Ref.
β-Ga_2O_3 (this work)	(100)	elliptic / hyperbolic	600-780	115	22.7 [010]	~3-6	This work
α-MoO_3	(010)	elliptic / hyperbolic	820-1010	250	11.7 [100] 9.3 [001]	>6	11
hBN	(001)	isotropic	1360-1610	20	13.5	>6	12
α-V_2O_5	(010)	elliptic / hyperbolic	750-1050	105	10.7 [100] 12.2 [001]	3.5	13
Gypsum ($CaSO_4 \cdot 2H_2O$)	(010)	elliptic / hyperbolic shear	1110-1209	75	25 [100] 10 [001]	–	6

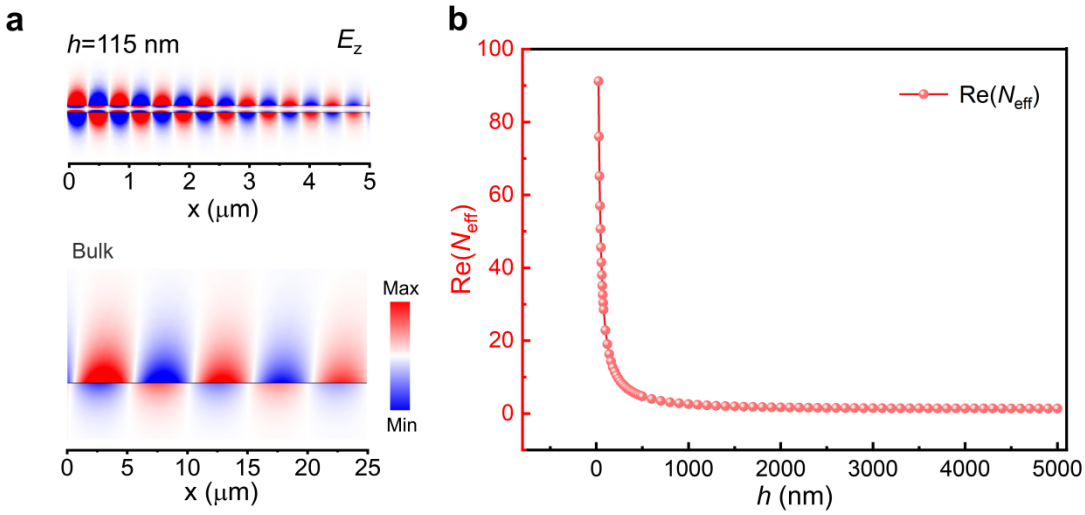

Fig. S1 Dimensional reduction induces extreme field confinement of polaritons. (a) Cross-sectional mode profile of phonon polaritons, the out-of-plane component of the optical field E_z is shown. Up: volume-confined mode within nanoflake. Down: surface mode within bulk crystal. (b) Field compression factor of the polariton mode at 715 cm^{-1} against increasing thickness of β-Ga_2O_3.

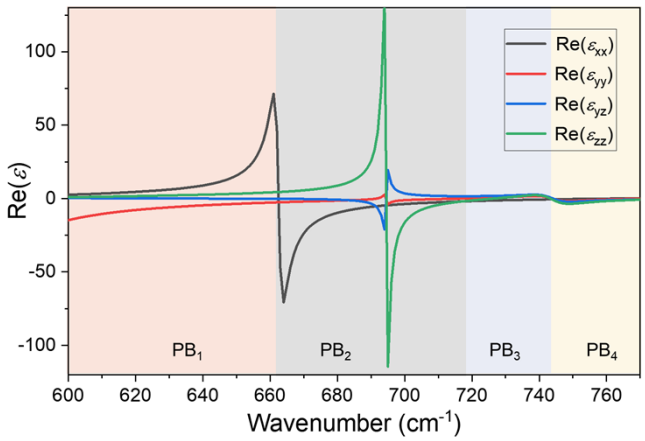

Fig. S2 Dielectric properties of (100)-oriented β-Ga_2O_3. Frequency-dependent real parts of the dielectric tensor components (Re(ε_{xx}), Re(ε_{yy}), Re(ε_{yz}), and Re(ε_{zz}) for (100) plane as *xy*-plane.

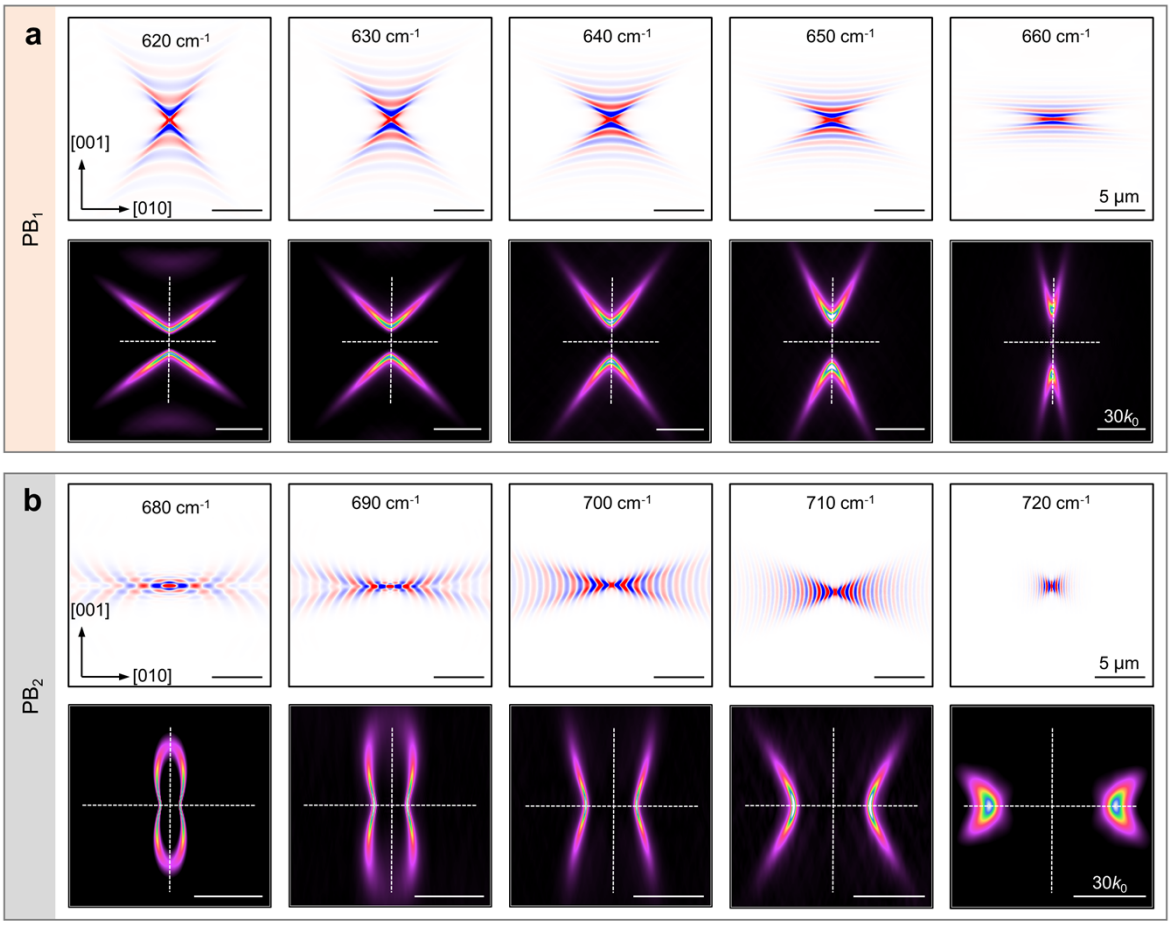

Fig. S3 Frequency-dependent hyperbolic polaritons in a suspended (100)-oriented β-Ga_2O_3 nanoflake across two different polariton bands. Near-field patterns (top) and corresponding Fourier-transformed isofrequency contours (IFCs, bottom) across two Reststrahlen bands show frequency-switchable hyperbolic polaritons: (a) In PB$_1$ (620–

663 cm^{-1}), polaritons propagate along the [001] axis. (b) In PB_2 (680–716 cm^{-1}), polaritons propagate along the [010] axis.

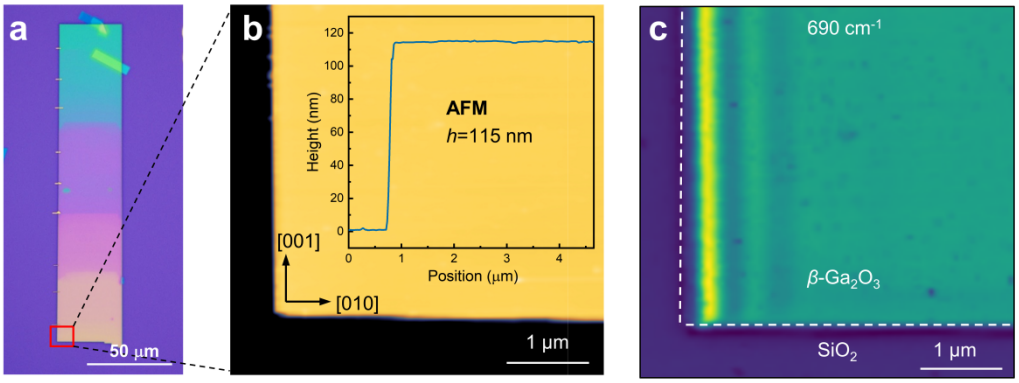

Fig. S4 CVD-grown (100)-oriented β-Ga_2O_3 nanoflakes with anisotropic polaritons. (a) Optical image of a rectangular nanoflake. Orthogonal edges align with crystal axes: short edge∥[010], long edge∥[001]. (b) AFM topography of the region boxed in (a), with height profile (insert) confirming uniform thickness (h = 115 nm). (c) Near-field optical image at 680 cm^{-1} showing polaritonic fringes parallel to [010], signature of hyperbolic confinement in PB_2.

The propagation wavevector (real part k') and attenuation coefficient (imaginary part k'') of the polaritons are obtained by analyzing the oscillatory decay of the near-field amplitude (S_2) as a function of the tip-to-source distance x (Fig. 5a). The spatial profile is fitted using a custom MATLAB script based on a one-dimensional damped oscillation model with a power-law prefactor:

$$S_2(x) = A \cdot e^{-k'x} \cdot \frac{cos(k''x + \varphi)}{x^{\beta}} + C$$

where A is the amplitude, φ is a phase offset, C is a constant background, and β is a power-law exponent that accounts for additional distance-dependent decay mechanisms. The propagation wavevector k' corresponds directly to the oscillation frequency, while the attenuation coefficient k'' quantifies the exponential decay rate of the polariton energy.

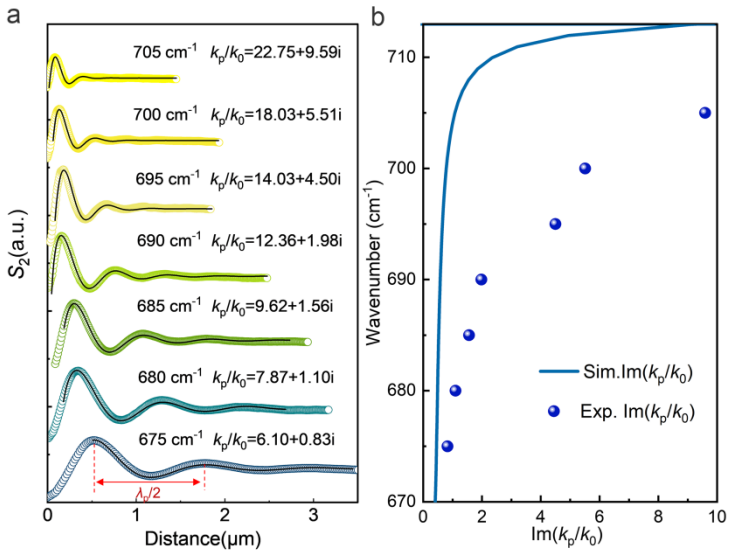

Fig. S5 (a) Line profiles of polaritonic interference fringes propagating along the [010] direction at different frequencies, as a function of the distance from the flake edge. $\lambda_p/2$: the polaritons excited by the tip propagate away and are back-reflected at the flake edges, giving rise to interference fringes. (b) Imaginary part of the polariton wavevector extracted from near-field fringe fitting (blue symbols) compared with the theoretical calculation (blue line). The dielectric function used in the calculation follows Refs. [14] and [15].

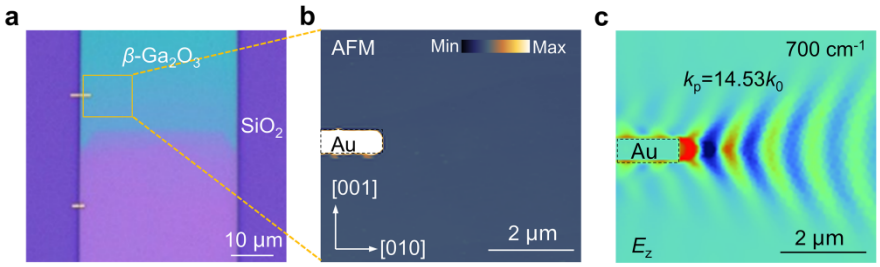

Fig. S6 (a) Optical microscope image of the β-Ga_2O_3 nanoflake shown in Fig. 3a. (b) Atomic force microscope image of the region marked by the orange box in (a). The flake thickness is 155 nm. Antenna dimensions: length, 1.5 μm; width, 500 nm; height, 100 nm. (c) Simulated polaritons launched by a gold antenna at 700 cm^{-1}, displaying divergent wavefronts. The dielectric function used in the calculation follows Refs. [14] and [15].

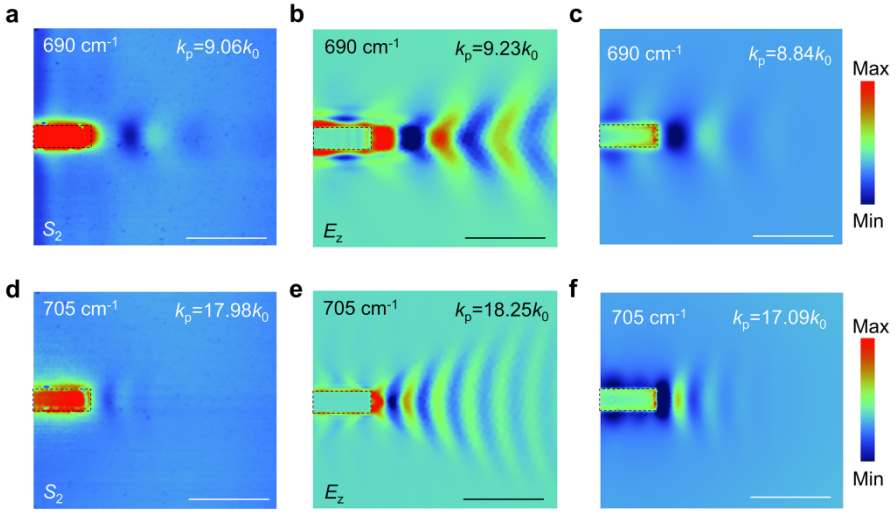

Fig. S7 Frequency-dependent hyperbolic polaritons excited by gold nanorod on a (100) β-Ga_2O_3 nanoflake. (a, d) Experimental near-field images (690 and 705 cm^{-1}) of gold-antenna-excited polaritons showing divergent wavefronts. (b, e) Simulated polariton patterns, using the standard dielectric function.[14, 15] (c, f) Simulated polariton patterns with the imaginary parts of the in-plane dielectric components (ε_{xx} and ε_{yy}) increased by a factor of six. Scale bar: 2 μm.

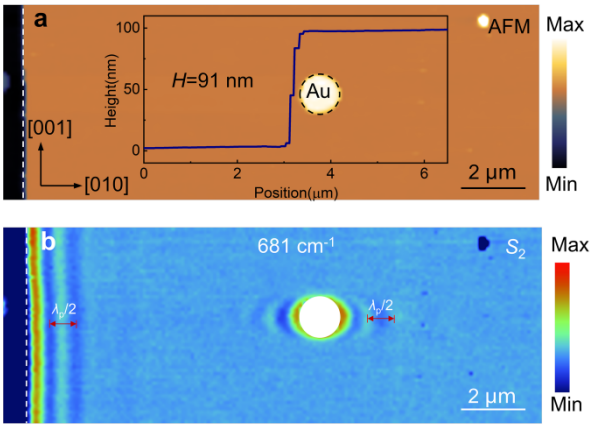

Fig. S8 Real-space focusing of polaritons by a gold disk on a 91 nm-thick β-Ga_2O_3 nanoflake. (a) AFM topography of the gold disk (radius: 650 nm; height: 60 nm) on the flake. (b) Experimental near-field image at 681 cm^{-1}, showing the focusing of polaritons by the disk.

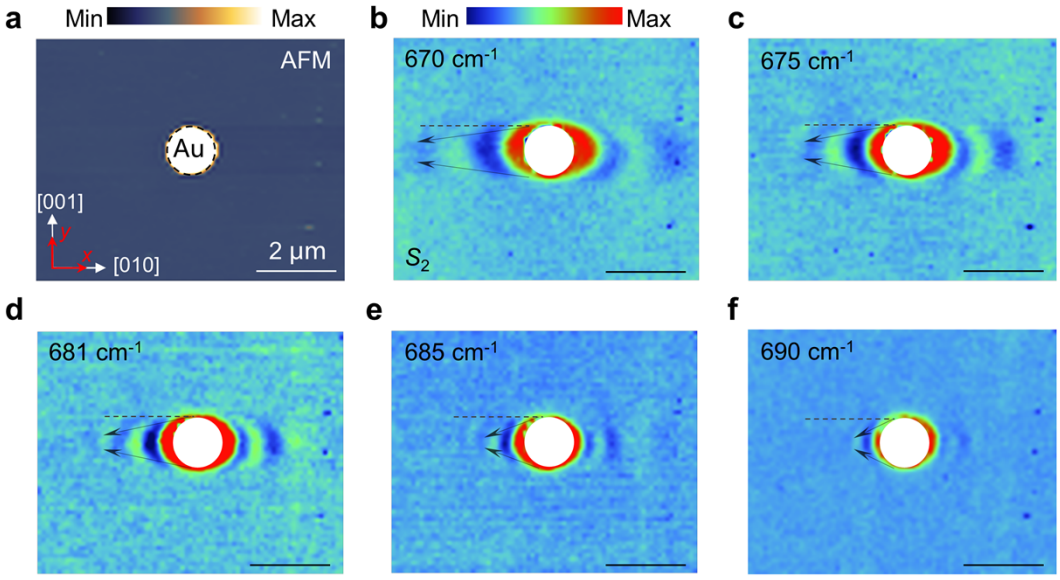

Fig. S9 Frequency-dependent focusing of phonon polaritons by a gold disk on a 91-nm-thick β-Ga_2O_3 nanoflake. (a) AFM topography of the gold disk. (b–f) Experimental near-field images showing polariton focusing by the gold disk at frequencies from 670 to 690 cm^{-1}.

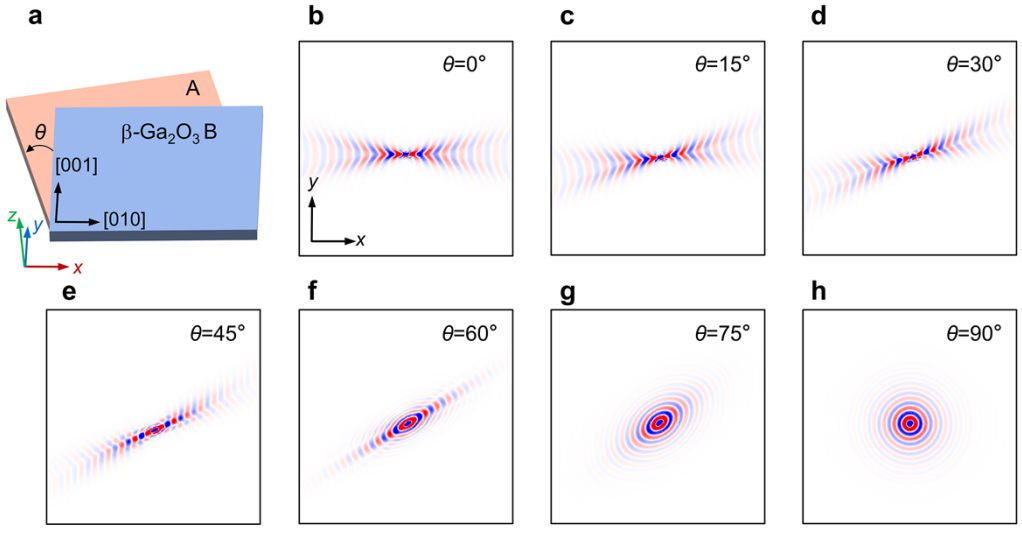

Fig. S10 Rotation-induced topological transition of phonon polaritons. (a) Schematic of twisted bilayer β-Ga_2O_3. Both the top layer (β-Ga_2O_3 B) and bottom layer (β-Ga_2O_3 A) are 60 nm thick. The *x* and *y* axes are aligned with the [010] and [001] crystallographic directions of the top layer (β-Ga_2O_3 B). The twist angle (θ) is defined as the counterclockwise rotation of the bottom layer (β-Ga_2O_3 A) relative to the top layer (β-Ga_2O_3 B). (b–h) Numerical simulations of the out-of-plane electric field component (E_z) distributions at 680 cm^{-1}, illustrating the phonon polariton topology evolution with twist angle. The bilayer's dispersion relation transitions from hyperbolic (θ = 15° to 45°) to elliptical (θ = 75°) and finally to isotropic (θ = 90°).

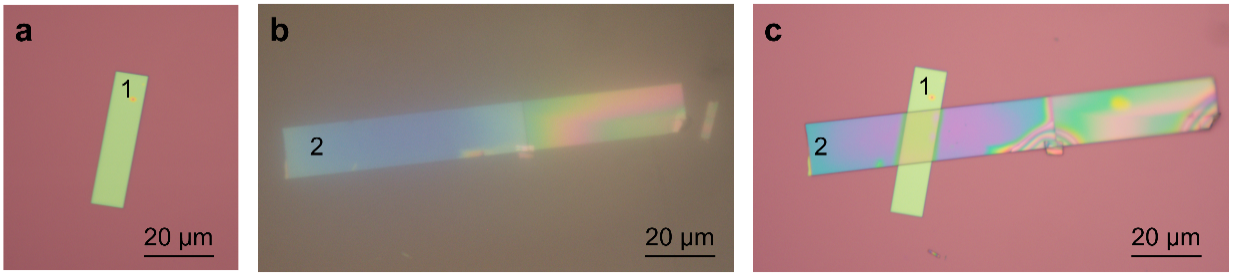

Fig. S11 Deterministic assembly of β-Ga_2O_3 bilayers via dry transfer method. (a) Bottom-layer β-Ga_2O_3 nanoflake on SiO_2/Si substrate. (b) Top-layer β-Ga_2O_3 nanoflake on PDMS substrate. (c) Stacked bilayer with controlled twist angle.

References

[1] Huang, Y., Pan, Y. H., Yang, R. et al. Universal mechanical exfoliation of large-area 2D crystals. Nat. Commun. 2020, 11 (1), 2453.

[2] [Mounet, N., Gibertini, M., Schwaller, P. et al. Two-dimensional materials from high-throughput computational exfoliation of experimentally known compounds. Nat. Nanotechnol. 2018, 13, 246.

[3] [Barman, S. K., Huda, M. N. Mechanism behind the easy exfoliation of Ga_2O_3 ultra-thin film along (100) surface. Phys. Status Solidi RRL 2019, 13, 1800554.

[4] Balan, A., Puthirath, A., Roy, S. et al. Non-van der Waals quasi-2D materials: recent advances in synthesis, emergent properties and applications. Mater. Today 2022, 58, 164.

[5] Xu, Y., Liu, K., Peng, G. et al. High-κ $KBe_2BO_3F_2$ dielectric material with wide bandgap for two-dimensional electronics. Nat. Commun. 2026.

[6] Díaz-Núñez, P., Lanza, C., Wang, Z. et al. Visualization of topological shear polaritons in gypsum thin films. Sci. Adv. 2025, 11 (29), eadw3452.

[7] Alam, M. S., Chowdhury, M. A., Kowser, M. A. et al. Advances of MAX phases: synthesis, characterizations and challenges. Eng. Rep. 2024, 6 (8).

[8] Khazaei, M., Wang, J., Estili, M. et al. Novel MAB phases and insights into their exfoliation into 2D MBenes. Nanoscale 2019, 11 (23), 11305-11314.

[9] Yang, H., Sun, H., Li, Q. et al. Structural, electronic, optical and lattice dynamic properties of the different WO_3 phases: first-principle calculation. Vacuum 2019, 164, 411-420.

[10] Jiang, K., Ji, J., Gong, W. et al. Mechanical cleavage of non-van der Waals structures towards two-dimensional crystals. Nat. Synth. 2023, 2, 58.W.

[11] Ma, W., Alonso-González, P., Li, S. et al. In-plane anisotropic and ultra-low-loss polaritons in a natural van der Waals crystal. Nature 2018, 562, 557.
[12] Dai, S., Fei, Z., Ma, Q. et al. Tunable phonon polaritons in atomically thin van der Waals crystals. Science, 2014, 343, 1125.
[13] Taboada-Gutiérrez, J., Álvarez-Pérez, G., Duan, J. et al. Broad spectral tuning of ultra-low-loss polaritons in a van der Waals crystal by intercalation. Nat. Mater. 2020, 19, 964.
[14] Schubert, M., Korlacki, R., Knight, S., et al. Anisotropy, phonon modes, and free charge carrier parameters in monoclinic β-gallium oxide single crystals. Phys. Rev. B 2016, 93, 125209.
[15] Passler, N., Ni, X., Hu, G. et al. Hyperbolic shear polaritons in low-symmetry crystals. Nature, 2022, 602, 595-600.